ACS MATERIALS LETTERS

www.acsmaterialsletters.org

LETTER

One-Step Synthesis of Two-Dimensional Metal–Semiconductor Circuitry Based on W-Triggered Spatial Phase Engineering

Yi Zeng, Shengqiang Wu, Xiaolong Xu, Biao Zhang, Bo Han, Zijing Zhao, Yu Pan, Feng Wang, Qi Wang, Yuqia Ran, Peng Gao, Xiaoxu Zhao,* Yu Ye,* and Yanglong Hou*

Cite This: *ACS Materials Lett.* 2023, 5, 2324–2331

Read Online

ACCESS | Metrics & More | Article Recommendations | Supporting Information

ABSTRACT: **Molybdenum ditelluride ($MoTe_2$) exhibits a variety of crystal phases, which can be phase-controlled by various external means, showing broad prospects in modern integrated circuits. The structure in which the semimetal 1T′ (or T_d) phase electrode contacts the semiconductor 2H phase channel is considered an elegant solution for high-performance two-dimensional (2D) circuits because it achieves low contact resistance. However, most of the 2D metal–semiconductor structures for large-area integration use a two-step growth process, which puts forward high requirements for the secondary growth compatibility of the material. Here, we develop a method for the stable synthesis of the metallic $Mo_xW_{1-x}Te_2$ ($0 < x < 1$) by W-triggered spatial phase engineering, and we further obtain a large-area $Mo_xW_{1-x}Te_2$/2H-$MoTe_2$ in-plane metal–semiconductor structure by one-step tellurization of a MoW/Mo periodic structure. Due to the unique 2D in-plane epitaxial mechanism of the phase transition from 1T′ to 2H, the highly crystalline semiconductor 2H-$MoTe_2$ squeezes between two metallic $Mo_xW_{1-x}Te_2$ electrodes and forms a seamless coplanar contacted channel; thus, the fabricated field-effect transistors exhibit good electrical characteristics. In addition, large-area 2D metal–semiconductor heterostructure arrays can be transferred onto flexible substrates, showing promising applications in flexible electronics. Herein, one-step synthesis of large-area 2D in-plane metal–semiconductor arrays opens up new possibilities for future integrated high-performance logic circuits.**

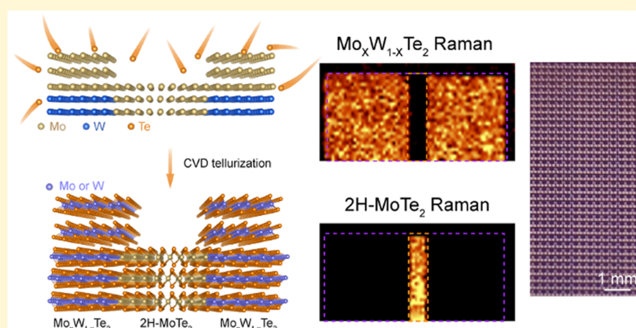

Downloaded via PEKING UNIV on November 17, 2023 at 07:33:29 (UTC).
See https://pubs.acs.org/sharingguidelines for options on how to legitimately share published articles.

Two-dimensional (2D) transition-metal dichalcogenides (TMDs) have attracted increasing attention owing to their diverse species,[1] tunable band gaps,[2,3] and numerous phase structures,[4,5] showing broad and promising application prospects in future flexible electronics and optoelectronics.[6,7] Different phase structures of $MoTe_2$ exhibit distinct physical properties, and various phase-engineering methods have been developed to achieve phase transition,[5,8] including thermal annealing,[9,10] laser radiation,[11] strain,[12,13] intercalation,[14] doping,[15] alloying,[16−18] and electric field[19] modulating methods. TMD-based 2D metal–semiconductor heterostructures exhibit ohmic contact behavior with low contact resistance, which is an effective approach for high-performance 2D electronics.[20,21] Therefore, the phase-controlled synthesis of large-scale 2D metal–semiconductor heterostructures based on TMDs shows promising applications. The existing phase-engineering methods usually suffer from poor spatial controllability, small-scale production, and poor material compatibility.[10−15,22−25] In addition, most of the 2D metal–semiconductor structures suitable for large-area integration use a two-step chemical vapor deposition (CVD) growth process,[26−30] which puts forward high requirements for the secondary growth compatibility of the materials. It is in tight demand to devise a spatially controlled and scalable one-step phase-engineering growth method for directly synthesizing metal–semiconductor heterostructure arrays of TMDs. Recently, large-scale 1T′/2H $MoTe_2$ metal–semiconductor heterostrucutres were obtained by one-step tellurizing MoO_3/$MoO_{2.0-2.5}$ patterns fabricated by a complex process (where the precursor for 1T′-$MoTe_2$ growth is MoO_3 film deposited

Received: June 19, 2023
Accepted: July 26, 2023
Published: July 29, 2023

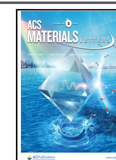

© 2023 American Chemical Society

https://doi.org/10.1021/acsmaterialslett.3c00654
ACS Materials Lett. 2023, 5, 2324–2331

by thermal evaporation, and the precursor for 2H-$MoTe_2$ growth is $MoO_{2.0-2.5}$ film obtained by magnetron sputtering of Mo film followed by oxidation).[31] Another one-step method for fabricating the in-plane 1T′/2H/1T′ $MoTe_2$ heterophases was phase-selective growth of specific molybdenum precursors Mo/MoO_3 (where the precursor for 1T′-$MoTe_2$ growth is a continuous Mo film prepared by electron beam evaporation, and the precursor for 2H-$MoTe_2$ growth is MoO_3 film prepared by treating Mo film with oxygen plasma).[25] Table S1 further summarized the detailed comparison of large-area fabrication parameters for different growth methods. Existing one-step methods are sensitive to the types of precursors and growth parameters. Besides, it is difficult to control or improve the crystallinity of the semiconducting channel, which, however, is the key to limiting its application.

In this work, we develop a stable W-triggered phase-engineering strategy and report the one-step growth of large-scale patterned metal−semiconductor 2D heterojunction arrays. Stable and spatially controllable phase engineering of $MoTe_2$ is realized by selective W alloying. High-angle annular dark-field scanning transmission electron microscopy (HAADF-STEM) and energy dispersive X-ray spectroscopy (EDX) characteristics show that the alloyed parts formed the metallic $Mo_xW_{1-x}Te_2$ ($0 < x < 1$). In the unalloyed region, electron backscattered diffraction (EBSD) illustrates the high crystallinity of the semiconducting channel due to the unique 1T′ to 2H phase transition mechanism in $MoTe_2$. Field-effect transistor (FET) arrays fabricated using heterostructures show good contact properties and outstanding promise as flexible electronic devices. This one-step growth of large-scale patterned 2D metal−semiconductor heterojunction arrays opens up new possibilities for future integrated high-performance logic circuits.

Theoretical calculations reveal that in monolayer $Mo_xW_{1-x}Te_2$ ($0 < x < 1$), the substitution of Mo by W changes the sign of energy difference between the 2H and 1T′ phases,[32] and extensive experimental works synthesized 1T′ or T_d phase $Mo_xW_{1-x}Te_2$ bulk crystals via W alloying.[16,17] Therefore, we propose a method to precisely control the $MoTe_2$ phase using a spatial W-triggered alloying strategy to realize 2D metal−semiconductor heterostructure arrays. Specifically, the periodic structure of MoW/Mo was first constructed by photolithography and magnetron sputtering, and $Mo_xW_{1-x}Te_2/MoTe_2$ heterostructures were obtained by one-step CVD tellurization (Figure 1). Pure Mo films are tellurized to 2H-$MoTe_2$, while Mo/W films are tellurized to metallic $Mo_xW_{1-x}Te_2$ alloys after CVD growth. Based on the calculated energy difference between 2H, 1T′ and T_d phases inTMDs, the energy of 2H-WTe_2 is much higher than that of 1T′,[33] making the synthesis of 2H-WTe_2 extremely difficult. Driven by the supply of Te atoms in CVD tellurization, the forming of $MoTe_2$ film undergoes a solid-to-solid phase transformation from metallic 1T′-$MoTe_2$ to semiconducting 2H-$MoTe_2$.[34] However, when the Mo/W region is tellurized, it tends to form a metallic phase rather than a semiconducting 2H phase, which is due to the introduction of W that makes the 2H phase much higher in energy than the 1T′ or T_d phases.

The detailed fabrication process of the large-scale patterned $Mo_xW_{1-x}Te_2/MoTe_2$ heterostructure arrays is shown in Figure 2. First, about 2 nm-thick rectangular W patterns were fabricated on SiO_2/Si substrates by photolithography, magnetron sputtering, and lift-off processes (Figure 2a,e) to define the

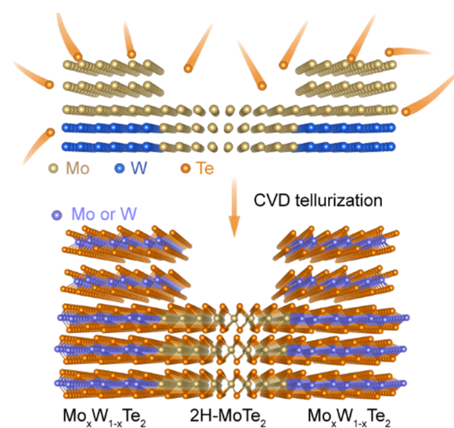

Figure 1. Schematic illustration of the one-step growth of the $Mo_xW_{1-x}Te_2/MoTe_2$ heterophase film using a spatial W-triggered phase engineering strategy.

regions that subsequently serve as 2D metal electrodes or wiring. Then, a ∼3 nm-thick continuous Mo film was deposited on the whole patterned substrate via magnetron sputtering (Figure 2b,f). Subsequently, the large-scale 2D metal−semiconductor heterophase film was synthesized via CVD tellurization using the substrate-facing-up or substrate face-to-face growth methods (Figure 2c,g), in which the rectangular Mo/W regions were tellurized into metallic $Mo_xW_{1-x}Te_2$, and elsewhere the pure Mo film was tellurized to a uniform and continuous 2H-$MoTe_2$ film (see detailed growth parameters in Supporting Information, the optical images of quartz tubes with different growth methods are shown in Figures S1 and S2). Finally, $Mo_xW_{1-x}Te_2$/2H-$MoTe_2$/$Mo_xW_{1-x}Te_2$ arrays were fabricated by photolithography and reactive ion etching (RIE) processes (Figure 2d,h). The W-triggered phase-engineering method has good planar resolution of the patterning (Figure S3 and S4), on the order of hundreds of nanometers, depending on the resolution of the lithography.

The W-triggered spatial phase engineering method shows good reproducibility and controllability. In different samples of the same batch and different batches, under proper growth temperature and time, the area deposited Mo/W will be tellurized into the $Mo_xW_{1-x}Te_2$ alloy, and the Mo film will be tellurized into the 2H-$MoTe_2$ film. For the Mo/W precursor, when the composition ranges from 3 nm-Mo/2 nm-W to 3 nm-Mo/20 nm-W, the growth temperature ranges from 580 to 650 °C, and the growth time ranges from 0.5 to 2 h, all of which are tellurized into metallic alloys. For the 2H-$MoTe_2$ film, when the thickness of the Mo film is 3 nm, the substrate-facing-up growth method can obtain full coverage of 2H-$MoTe_2$ at 620−650 °C for 1.5−2 h. Using the substrate face-to-face growth method,[35] the growth temperature and time can be reduced to 580 °C and 1 h, and a fully covered 2H-$MoTe_2$ film can be obtained.

The synthesis of 2H-$MoTe_2$ thin films is understood as nucleation and subsequent in-plane epitaxial growth through 1T′- to 2H-$MoTe_2$ solid-to-solid phase transformation.[34] To study the growth kinetics of the heterostructures, we shortened the growth time of the substrate-facing-up growth method from 2 to 1 h to obtain partially phase-transformed $MoTe_2$ thin film (Figure 3a). Outside the patterned W regions (which have been tellurized to $Mo_xW_{1-x}Te_2$), 2H-$MoTe_2$ domains form in the background of 1T′-$MoTe_2$ and expand out until they

https://doi.org/10.1021/acsmaterialslett.3c00654
ACS Materials Lett. 2023, 5, 2324−2331

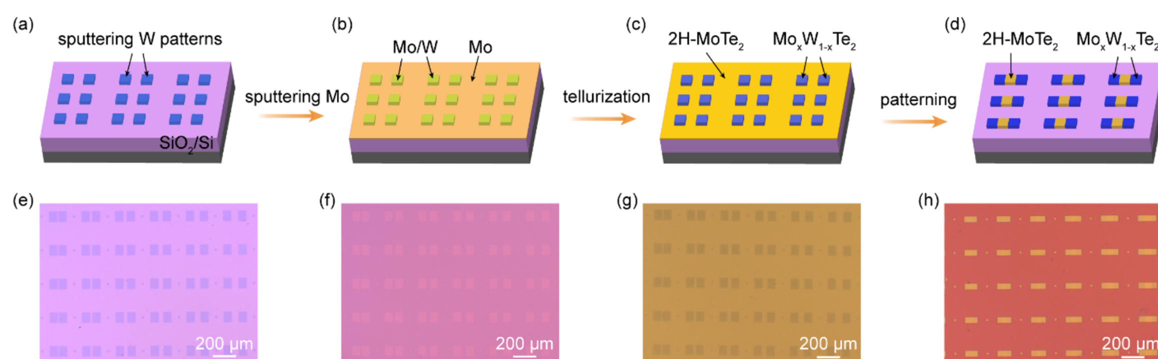

Figure 2. Schematic illustration of the one-step growth processes of the $Mo_xW_{1-x}Te_2$/2H-$MoTe_2$ heterophase arrays and corresponding optical images. (a, e) Large-scale rectangular W patterns were fabricated by photolithography, magnetron sputtering, and lift-off processes on a SiO_2/Si substrate. (b, f) Full coverage Mo film was deposited via magnetron sputtering. (c, g) Large-scale $Mo_xW_{1-x}Te_2$/2H-$MoTe_2$ heterophase film was obtained via CVD tellurization. (d, h) Large-scale $Mo_xW_{1-x}Te_2$/2H-$MoTe_2$/$Mo_xW_{1-x}Te_2$ arrays were fabricated by photolithography and RIE processes.

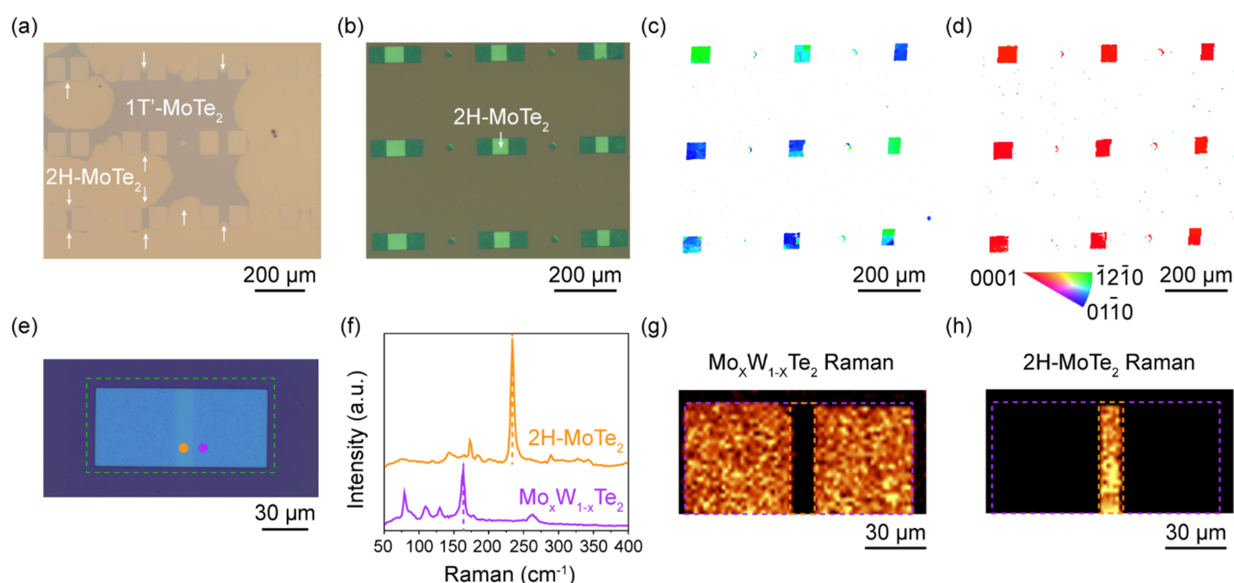

Figure 3. EBSD and Raman characterizations of the $Mo_xW_{1-x}Te_2$/2H-$MoTe_2$ heterophase. (a) Optical image of the partially phase transformed film. The white arrows indicate the growth directions of 2H-$MoTe_2$. (b) Optical image of a 3 × 3 $Mo_xW_{1-x}Te_2$/2H-$MoTe_2$ heterostructure array. (c) The transverse IPF map of the heterostructure shown in (b). (d) Phase distribution map at the same region. (e) Optical image of a representative $Mo_xW_{1-x}Te_2$/2H-$MoTe_2$ heterostructure. The orange and purple dots represent channel and electrode regions, respectively, for Raman spectra acquisition. (f) Raman spectra at the channel and electrode regions, respectively. The orange and purple dashed lines represent the characteristic Raman peaks of 2H-$MoTe_2$ and $Mo_xW_{1-x}Te_2$ used for Raman mappings, respectively. (g, h) Raman mappings of the $Mo_xW_{1-x}Te_2$ 161 cm^{-1} peak and 2H-$MoTe_2$ 233 cm^{-1} peak at the corresponding region labeled by the green dashed box in (e), respectively.

encounter the $Mo_xW_{1-x}Te_2$ edges. In the narrow channel defined by the $Mo_xW_{1-x}Te_2$ patterns, we can see that 2H-$MoTe_2$ domains squeeze into the channel and grow forward (indicated by the white arrows in Figure 3a) until long enough tellurization time to form the fully transformed 2H-$MoTe_2$ film, which ensures high crystallinity of the semiconducting channel. The crystallinity of the semiconducting channel 2H-$MoTe_2$ was investigated by EBSD, and the crystallinity characterizations of the as-grown $Mo_xW_{1-x}Te_2$/2H-$MoTe_2$ heterophase film are shown in Figure S5. Figure 3b shows the optical image of a 3 × 3 $Mo_xW_{1-x}Te_2$/2H-$MoTe_2$ heterostructure array, and its corresponding in-plane transverse inverse pole figure (IPF) map shows that the 2H-$MoTe_2$ channel exhibits a single color or is stitched by two colors (Figure 3c), indicating that the channel is formed by the 2H-$MoTe_2$ single crystal or splicing of two crystal domains. The phase-distribution map (Figure 3d) related to the 2H phase (0001 crystal orientation) shows a uniform red color, indicating that the channel is a continuous pure 2H phase. Due to the poor conductivity of the SiO_2/Si substrate and long scan time, the IPF and phase-distribution maps are slightly distorted compared to the optical image.

Raman spectroscopy was employed to confirm the composition of each region in the heterostructure (Figure 3e). The Raman spectrum of the electrode region shows a series of peaks at ~76 cm^{-1}, ~107 cm^{-1}, ~127 cm^{-1}, ~161 cm^{-1} and ~260 cm^{-1} (Figure 3f), consistent with previously reported Raman spectra of bulk 1T′-$Mo_xW_{1-x}Te_2$,[17] suggesting that Mo/W patterns were tellurized to 1T′-$Mo_xW_{1-x}Te_2$ ($0 < x < 1$) alloys. The channel is confirmed to be 2H-$MoTe_2$ by the appearance of the well-resolved Raman peaks at ~172 cm^{-1} (A_g mode), ~233 cm^{-1} (E^1_{2g} mode), and ~289 cm^{-1} (B^1_{2g}

https://doi.org/10.1021/acsmaterialslett.3c00654
ACS Materials Lett. 2023, 5, 2324−2331

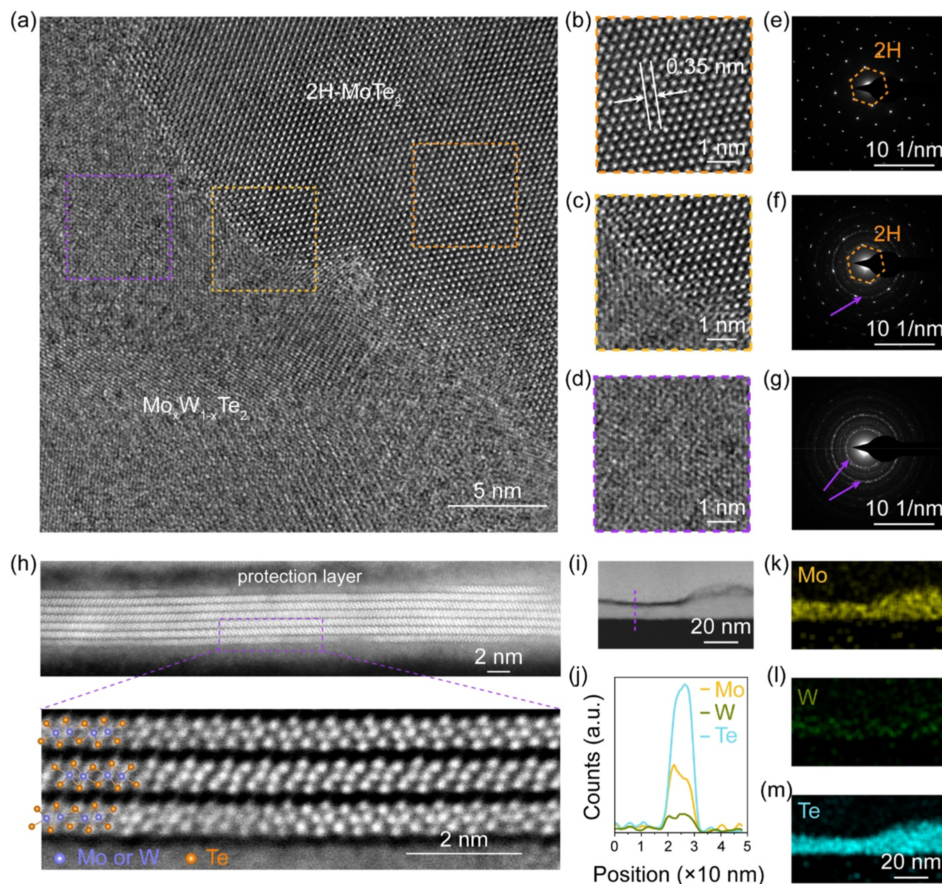

Figure 4. TEM characterizations of the $Mo_xW_{1-x}Te_2$/2H-$MoTe_2$ heterophase. (a) HRTEM image at the $Mo_xW_{1-x}Te_2$/2H-$MoTe_2$ heterophase interface region. (b−d) Zoomed-in HRTEM images of the 2H-$MoTe_2$ semiconducting channel region, heterophase interface region, and $Mo_xW_{1-x}Te_2$ metal electrode region labeled by the dashed boxes in (a), respectively. (e−g) SAED patterns of the 2H-$MoTe_2$ region, heterophase interface region, and $Mo_xW_{1-x}Te_2$ region, respectively. (h) Atomic-resolution cross-sectional HAADF-STEM image of the 1T′-$Mo_xW_{1-x}Te_2$ region with the corresponding atomic structure model superimposed. (i) Low-magnification cross-sectional HAADF-STEM image of the $Mo_xW_{1-x}Te_2$ region. (j) EDX line profiles of Mo, W, and Te elements along the purple dashed line labeled in (i). (k−m) Cross-sectional EDX mappings of the Mo, W, and Te elements of the $Mo_xW_{1-x}Te_2$ region shown in (i), respectively.

mode). The Raman mappings of the $Mo_xW_{1-x}Te_2$ 161 cm^{-1} peak and 2H-$MoTe_2$ 233 cm^{-1} peak show uniform signals in the contact and channel regions, respectively, with clear and distinct interfaces (Figure 3g,h). It is the same as the Raman mappings of $Mo_xW_{1-x}Te_2$ with the peak at 76 cm^{-1} (Figure S6). The as-grown $Mo_xW_{1-x}Te_2$ and 2H-$MoTe_2$ films have a thickness of 13.6 and 9.2 nm, respectively (Figure S7), and a roughness of 1.5−2.2 nm.

We further analyze the composition and crystallinity of the heterophase film using electron microscopy techniques. High-resolution transmission electron microscopy (HRTEM) image shows the interface consists of polycrystalline monoclinic (1T′) structure domains of about tens of nanometers seamlessly contacted to a single hexagonal (2H) structure domain (Figure 4a−d). The hexagonal structure of the semiconducting channel shows an atomic spacing of about 0.35 nm (Figure 4b), which is consistent with the lattice constant of 2H-$MoTe_2$. The corresponding selected area electron diffraction (SAED) pattern recorded in the 2H region shows a single set of sharp 6-fold symmetric diffraction spots (Figure 4e), suggesting the single-crystal nature of 2H-$MoTe_2$, which is consistent with EBSD results. The typical SAED at the heterophase interface consists of a single set of diffraction spots with 6-fold symmetry and a series of diffraction rings (Figure 4f), corresponding to single-crystalline 2H-$MoTe_2$ and polycrystalline $Mo_xW_{1-x}Te_2$, respectively. The SAED pattern from the $Mo_xW_{1-x}Te_2$ region shows only a series of diffraction rings (Figure 4g), indicating a polycrystalline nature. The structure of the polycrystalline metal part can not be identified by the HRTEM characterization from a top view (Figure S8). To further determine the crystal structure and composition of the electrode region, we performed cross-sectional STEM characterization. The image of the electrode region shows a clear layered structure with a layer spacing of ∼0.73 nm (Figure 4h). The van der Waals material exhibits a typical 1T′ phase atomic structure and stacking order (see the superimposed atomic structure diagram in zoomed-in Figure 4h). The cross-sectional HAADF-STEM image of the interface shows that the two $Mo_xW_{1-x}Te_2$ and 2H-$MoTe_2$ phases contacted seamlessly (Figure S9), consistent with the HRTEM image at the interface from the top view (Figure 4a), and we prepared the sample with thicker W film (∼10 nm) and 3 nm Mo film to find the interface clearly. The corresponding EDX line scan curves of Mo, W, and Te elements show that the three components are uniformly distributed in the vertical direction without delamination (Figure 4i, j). EDX mappings of Mo, W, and Te elements show that Mo and W are uniformly distributed in the tellurized material (Figure 4k−m), further

https://doi.org/10.1021/acsmaterialslett.3c00654
ACS Materials Lett. 2023, 5, 2324−2331

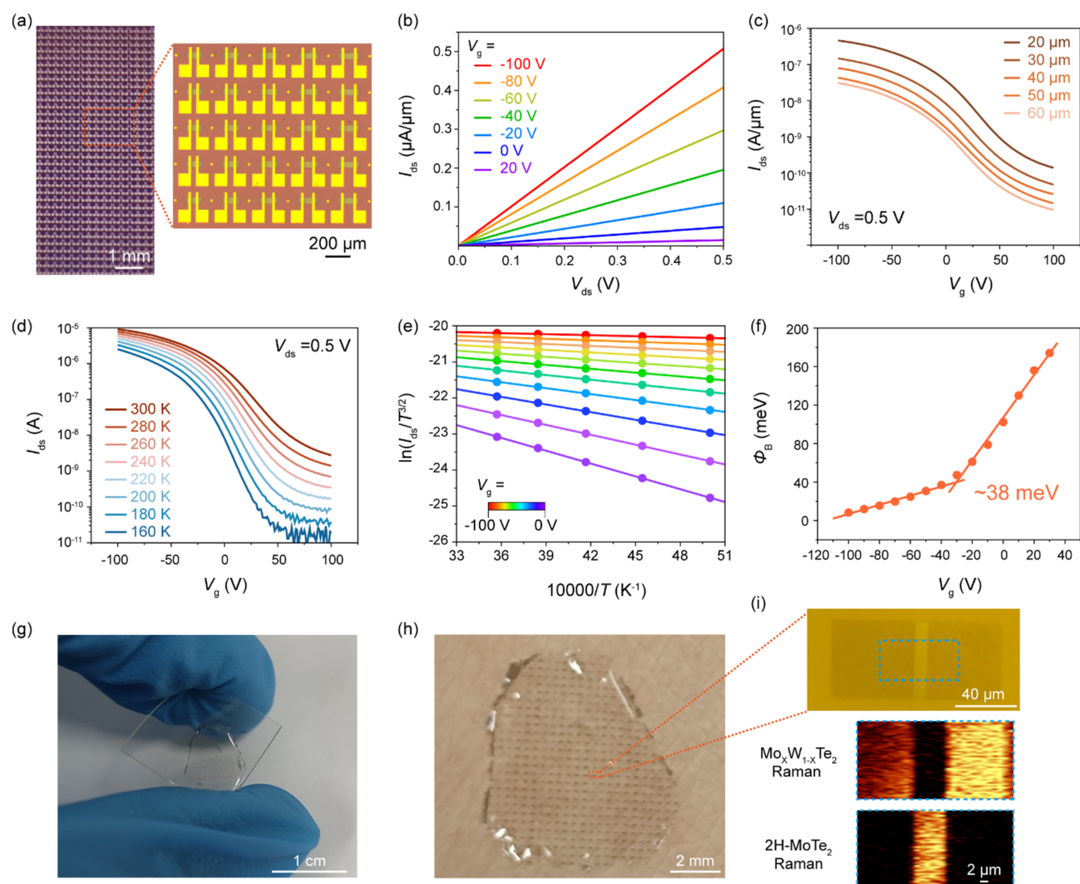

Figure 5. Electrical characterizations of the heterophase FET devices. (a) Optical image of the large-scale $Mo_xW_{1-x}Te_2$/2H-$MoTe_2$ heterophase FET arrays. (b) Typical room temperature I_{ds}-V_{ds} curves of FET measured at various gate voltages. (c) Typical room temperature transfer curves of the FETs with different channel lengths. (d) Temperature-dependent I_{ds}-V_g transfer curves of the FET. (e) Arrhenius plot under various gate voltages; the slope of the lines yields gate-voltage-dependent Φ_B. (f) The extracted gate-voltage-dependent effective Schottky barrier, Φ_B. (g) Free-standing $Mo_xW_{1-x}Te_2$/2H-$MoTe_2$/$Mo_xW_{1-x}Te_2$ heterostructure arrays transferred onto a flexible substrate. (h) Heterostructure arrays on PMMA film attached to human skin. (i) Optical and Raman mappings (representative Raman peaks from $Mo_xW_{1-x}Te_2$ and 2H-$MoTe_2$) images of a $Mo_xW_{1-x}Te_2$/2H-$MoTe_2$/$Mo_xW_{1-x}Te_2$ heterostructure on a PMMA film.

illustrating the formation of the $Mo_xW_{1-x}Te_2$ alloy, which matches with the Raman results.

$Mo_xW_{1-x}Te_2$ alloys usually exhibit 1T′ and T_d phases, and the energy difference between these two phases is very small. Therefore, alternate arrangements of these two phases in planar and vertical directions are common, and it is challenging to further distinguish the two phases of $Mo_xW_{1-x}Te_2$ alloys. In addition, the 1T′ and T_d phases of $Mo_xW_{1-x}Te_2$ alloys are both metallic, and as electrode materials, they do not significantly affect the electrical properties of the field-effect transistors.

We characterized the electrical properties of the as-grown $Mo_xW_{1-x}Te_2$ and 2H-$MoTe_2$ films (Figure S10 and S11), $Mo_xW_{1-x}Te_2$ is metallic and the transfer curves of $Mo_xW_{1-x}Te_2$ FETs with different channel lengths do not show any back-gate voltage dependence. 2H-$MoTe_2$ is semiconducting, and the transfer curves of 2H-$MoTe_2$ FETs contacted by Pd/Au show an on/off ratio of about 2 orders of magnitude with a mobility of ~1 cm^2 V^{-1} s^{-1}. To compare the resistivities of the two films, we measured typical I−V curves of the 2H-$MoTe_2$ and $Mo_xW_{1-x}Te_2$ devices using a four-terminal measurement method (Figure S12). The 9.2 nm thick, 50 μm wide, and 20 μm long 2H-$MoTe_2$ channel has a resistance of 1.02×10^7 Ω, so the room-temperature resistivity of 2H-$MoTe_2$ is 0.23 Ω·m. The resistance of a 13.6 nm thick $Mo_xW_{1-x}Te_2$ device with the same length and width is 260 Ω, so the room-temperature resistivity of $Mo_xW_{1-x}Te_2$ is 8.84×10^{-6} Ω·m. We compared the electrical properties of 2H-$MoTe_2$ channels contacted by Pd/Au electrodes and metallic $Mo_xW_{1-x}Te_2$ at room temperature (Figure S13), and the source-drain current of $Mo_xW_{1-x}Te_2$ contacted 2H-$MoTe_2$ device is higher than that of Pd/Au contacted 2H-$MoTe_2$ device at the same source drain voltage, where the on-current is about 1 order of magnitude higher and the on/off ratio is about 2 orders of magnitude larger.

To explore the electrical characteristics of the metal−semiconductor heterophase, centimeter-scale field-effect transistor arrays with different channel lengths were fabricated (Figure 5a). 2H-$MoTe_2$ serves as the semiconducting channel with $Mo_xW_{1-x}Te_2$ alloys on both sides as contact electrodes, and Pd/Au electrodes that are deposited on the $Mo_xW_{1-x}Te_2$ contacts are used as the external connections. Typical source-drain current (I_{ds}) versus source-drain voltage (V_{ds}) curves at different gate voltages all show linear output characteristics at room temperature (Figure 5b), confirming the ohmic contact with a low contact barrier between $Mo_xW_{1-x}Te_2$ and 2H-$MoTe_2$. Figure 5c shows the transfer curves of FETs with different channel lengths, showing p-type transistor characteristics with an on/off ratio of ~$10^{3.5}$ at a bias voltage of 0.5 V, the current decreases linearly with increasing channel length, indicating good device contact, superior to that of direct Pd/

https://doi.org/10.1021/acsmaterialslett.3c00654
ACS Materials Lett. 2023, 5, 2324−2331

Au metal contact.[27] The typical I_{ds}-V_g transfer curves at different bias voltages are shown in Figure S14, and the on/off ratio measured at room temperature does not change with different channel lengths (Figure S15). The field-effect mobilities of the $Mo_xW_{1-x}Te_2$ contacted 2H-$MoTe_2$ devices with various channel lengths are ~6.3 $cm^2\ V^{-1}\ s^{-1}$ (Figure S16). To evaluate the contact characteristics of the devices, we measured the temperature-dependent transfer curves from the FET with a channel length of 20 μm and extracted the Schottky barrier height (Figure 5d). The FET on/off ratio increases with decreasing temperature and reaches ~10^5 at 180 K. The barrier height, Φ_B, is extracted from the slope of the Arrhenius plot, that is, $\ln(I_{ds}/T^{3/2})$ versus $1/T$ (Figure 5e), yielding a back-gate-voltage-dependent barrier height (Figure 5f). The extracted Φ_B of the $Mo_xW_{1-x}Te_2$/2H-$MoTe_2$ heterophase contact is about 38 meV, which is lower than that of the Pd/Au contact (~200 meV).[31] Moreover, the large-area heterostructure arrays can be easily transferred onto flexible substrates by a PMMA-assisted wet transfer method (Figure 5g). The self-standing heterostructure arrays can also be transferred and attached conformally to the human skin (Figure 5h). Optical and Raman mapping images of the transferred heterostructure show an intact shape (Figure 5i), which shows great promise for future flexible electronics.

In summary, we developed a stable W-triggered phase-engineering method to synthesize large-scale patterned atomically scale $Mo_xW_{1-x}Te_2$/2H-$MoTe_2$ heterophase arrays in one step. HAADF-STEM, EDX, and Raman characteristics show that the W alloying strategy can form a stable metallic $Mo_xW_{1-x}Te_2$. Due to the unique 2D in-plane epitaxial mechanism of the phase transition from 1T′ to 2H, the highly crystalline semiconductor 2H-$MoTe_2$ squeezes between two metallic $Mo_xW_{1-x}Te_2$ electrodes and forms a seamless coplanar contacted channel. The FET devices fabricated by using the heterophase structures exhibit good electrical properties and good contact properties. Large-area heterostructure arrays can be further transferred onto flexible substrates, showing the potential applications of this strategy in flexible electronics. Our findings pave the way for the one-step construction of large-scale patterned flexible logical circuits.

■ ASSOCIATED CONTENT

Supporting Information

The Supporting Information is available free of charge at https://pubs.acs.org/doi/10.1021/acsmaterialslett.3c00654.

> Experimental details; Supplementary figures including optical images of quartz tubes with different growth methods, atomic force microscope images, scanning electron microscope images, EBSD characterizations, Raman result, HRTEM image, electrical results; Table of large-area fabrication parameters comparisons (PDF)

■ AUTHOR INFORMATION

Corresponding Authors

Yanglong Hou − *School of Materials Science and Engineering, Beijing Key Laboratory for Magnetoelectric Materials and Devices, Beijing Innovation Center for Engineering Science and Advanced Technology, Peking University, Beijing 100871, China;* orcid.org/0000-0003-0579-4594; Email: hou@pku.edu.cn

Yu Ye − *School of Physics and State Key Laboratory for Mesoscopic Physics and Frontiers Science Center for Nano-optoelectronics, Peking University, Beijing 100871, China;* orcid.org/0000-0001-6046-063X; Email: ye_yu@pku.edu.cn

Xiaoxu Zhao − *School of Materials Science and Engineering, Beijing Key Laboratory for Magnetoelectric Materials and Devices, Beijing Innovation Center for Engineering Science and Advanced Technology, Peking University, Beijing 100871, China;* orcid.org/0000-0001-9746-3770; Email: xiaoxuzhao@pku.edu.cn

Authors

Yi Zeng − *School of Materials Science and Engineering, Beijing Key Laboratory for Magnetoelectric Materials and Devices, Beijing Innovation Center for Engineering Science and Advanced Technology, Peking University, Beijing 100871, China; State Key Laboratory for Mesoscopic Physics and Frontiers Science Center for Nano-optoelectronics, Peking University, Beijing 100871, China;* orcid.org/0000-0003-1364-6137

Shengqiang Wu − *School of Materials Science and Engineering, Beijing Key Laboratory for Magnetoelectric Materials and Devices, Beijing Innovation Center for Engineering Science and Advanced Technology, Peking University, Beijing 100871, China*

Xiaolong Xu − *School of Physics and State Key Laboratory for Mesoscopic Physics and Frontiers Science Center for Nano-optoelectronics, Peking University, Beijing 100871, China;* orcid.org/0000-0003-2657-9658

Biao Zhang − *School of Materials Science and Engineering, Beijing Key Laboratory for Magnetoelectric Materials and Devices, Beijing Innovation Center for Engineering Science and Advanced Technology, Peking University, Beijing 100871, China*

Bo Han − *School of Physics and Electron Microscopy Laboratory and International Center for Quantum Materials, Peking University, Beijing 100871, China*

Zijing Zhao − *School of Materials Science and Engineering, Beijing Key Laboratory for Magnetoelectric Materials and Devices, Beijing Innovation Center for Engineering Science and Advanced Technology, Peking University, Beijing 100871, China*

Yu Pan − *School of Physics and State Key Laboratory for Mesoscopic Physics and Frontiers Science Center for Nano-optoelectronics, Peking University, Beijing 100871, China*

Feng Wang − *National Center for Nanoscience and Technology, Beijing 100190, China*

Qi Wang − *School of Physics and State Key Laboratory for Mesoscopic Physics and Frontiers Science Center for Nano-optoelectronics, Peking University, Beijing 100871, China*

Yuqia Ran − *School of Physics and State Key Laboratory for Mesoscopic Physics and Frontiers Science Center for Nano-optoelectronics, Peking University, Beijing 100871, China*

Peng Gao − *School of Physics and Electron Microscopy Laboratory and International Center for Quantum Materials, Peking University, Beijing 100871, China;* orcid.org/0000-0003-0860-5525

Complete contact information is available at: https://pubs.acs.org/10.1021/acsmaterialslett.3c00654

Author Contributions

Y.Z., Y.Y. and Y.H. conceived of the project and designed the experiments. Y.Z. synthesized the large-scale patterned 2D heterojunction arrays, characterized the heterojunction arrays,

fabricated the devices, and performed the electrical measurements. S.W. conducted the HAADF-STEM and EDX characterizations under the direction of X.Zh. X.X., Y.P., Q.W. and Y.R. performed the magnetron sputtering. B.H. conducted the HRTEM and SAED characterizations under the direction of P.Ga. F.W. assisted Y.Z. with the temperature-dependent electrical measurements. B.Z. draw the schematic diagram of the mechanism, Z.Z. provided useful discussions. Y.Y. and Y.H. supervised this research. Y.Z., Y.Y. and Y.H. wrote the manuscript. All authors contributed to discussions. CRediT: **Yi Zeng** conceptualization, data curation, formal analysis, investigation, methodology, resources, validation, visualization, writing-original draft, writing-review & editing; **Shengqiang Wu** investigation; **Xiaolong Xu** resources, writing-review & editing; **Biao Zhang** investigation, visualization; **Bo Han** investigation; **Zijing Zhao** investigation, writing-review & editing; **Yu Pan** resources; **Feng Wang** investigation; **Qi Wang** resources; **Yuqia Ran** resources; **Peng Gao** investigation; **Xiaoxu Zhao** formal analysis, funding acquisition, investigation, supervision, validation, writing-review & editing; **Yu Ye** conceptualization, formal analysis, funding acquisition, methodology, supervision, writing-review & editing; **Yanglong Hou** conceptualization, funding acquisition, project administration, supervision, writing-review & editing.

Notes

The authors declare no competing financial interest.

■ ACKNOWLEDGMENTS

This work was supported financially by the National Natural Science Foundation of China (Grants No. 52027801, 52111530236, 92263203), the National Key Research and Development Program of China (Grant No. 2017YFA0206301), the China-Germany Collaboration Project (Grant No. M-0199), the Key Research Program of Frontier Sciences, CAS (Grant No. ZDBS-LY-JSC015), the Beijing Natural Science Foundation (Grant No. JQ21018), and Emerging Engineering Interdisciplinary Project, Peking University, the Fundamental Research Funds for the Central Universities. The authors acknowledge the Electron Microscopy Laboratory in Peking University for the use of Cs corrected electron microscope. This work was supported by the Peking Nanofab.

■ REFERENCES

(1) Zhou, J. D.; Lin, J. H.; Huang, X. W.; Zhou, Y.; Chen, Y.; Xia, J.; Wang, H.; Xie, Y.; Yu, H. M.; Lei, J. C.; Wu, D.; Liu, F. C.; Fu, Q. D.; Zeng, Q. S.; Hsu, C.; Yang, C. L.; Lu, L.; Yu, T.; Shen, Z. X.; Lin, H.; Yakobson, B.; Liu, Q.; Suenaga, K.; Liu, G. T.; Liu, Z. A library of atomically thin metal chalcogenides. *Nature* **2018**, *556*, 355−359.

(2) Susarla, S.; Kutana, A.; Hachtel, J.; Kochat, V.; Apte, A.; Vajtai, R.; Idrobo, J. C.; Yakobson, B.; Tiwary, C. S.; Ajayan, P. M. Quaternary 2D transition metal dichalcogenides (TMDs) with tunable bandgap. *Adv. Mater.* **2017**, *29*, 1702457.

(3) Zeng, Q. S.; Wang, H.; Fu, W.; Gong, Y. J.; Zhou, W.; Ajayan, P.; Lou, J.; Liu, Z. Band engineering for novel two-dimensional atomic layers. *Small* **2015**, *11*, 1868.

(4) Deng, Y.; Zhao, X. X.; Zhu, C.; Li, P. L.; Duan, R. H.; Liu, G. T.; Liu, Z. $MoTe_2$: Semiconductor or Semimetal? *ACS Nano* **2021**, *15*, 12465−12474.

(5) Li, W. B.; Qian, X. F.; Li, J. Phase transitions in 2D materials. *Nat. Rev. Mater.* **2021**, *6*, 829.

(6) Wang, F. K.; Pei, K.; Li, Y.; Li, H. Q.; Zhai, T. Y. 2D Homojunctions for electronics and optoelectronics. *Adv. Mater.* **2021**, *33*, 2005303.

(7) Wu, M.; Xiao, Y. H.; Zeng, Y.; Zhou, Y. L.; Zeng, X. B.; Zhang, L. N.; Liao, W. G. Synthesis of two-dimensional transition metal dichalcogenides for electronics and optoelectronics. *InfoMater.* **2021**, *3*, 362−396.

(8) Zhang, H. Z.; Xu, C. Y.; Nan, H. Y.; Xiao, S. Q.; Gu, X. F. Research progress of two-dimensional transition metal dichalcogenide phase transition methods. *Acta Phys. Sin.* **2020**, *69*, 246101.

(9) Keum, D. H.; Cho, S.; Kim, J. H.; Choe, D.; Sung, H.; Kan, M.; Kang, H. Y.; Hwang, J.; Kim, S. W.; Yang, H.; Chang, K. J.; Lee, Y. H. Bandgap opening in few-layered monoclinic $MoTe_2$. *Nat. Phys.* **2015**, *11*, 482−486.

(10) Tan, Y.; Luo, F.; Zhu, M. J.; Xu, X. L.; Ye, Y.; Li, B.; Wang, G.; Luo, W.; Zheng, X. M.; Wu, N. N.; Yu, Y. Y.; Qin, S. Q.; Zhang, X. Controllable 2H-to-1T′ phase transition in few-layer $MoTe_2$. *Nanoscale* **2018**, *10*, 19964−19971.

(11) Cho, S.; Kim, S.; Kim, J. H.; Zhao, J.; Seok, J.; Keum, D. H.; Baik, J.; Choe, D.; Chang, K. J.; Suenaga, K.; Kim, S. W.; Lee, Y. H.; Yang, H. Phase patterning for ohmic homojunction contact in MoTe2. *Science* **2015**, *349*, 625−628.

(12) Song, S.; Keum, D. H.; Cho, S.; Perello, D.; Kim, Y.; Lee, Y. H. Room temperature semiconductor-metal transition of $MoTe_2$ thin films engineered by strain. *Nano Lett.* **2016**, *16*, 188−193.

(13) Hou, W.; Azizimanesh, A.; Sewaket, A.; Pena, T.; Watson, C.; Liu, M.; Askari, H.; Wu, S. M. Strain-based room-temperature non-volatile $MoTe_2$ ferroelectric phase change transistor. *Nat. Nanotechnol.* **2019**, *14*, 668.

(14) Eshete, Y. A.; Ling, N.; Kim, S.; Kim, D.; Hwang, G.; Cho, S.; Yang, H. Vertical heterophase for electrical, electrochemical, and mechanical manipulations of layered $MoTe_2$. *Adv. Funct. Mater.* **2019**, *29*, 1904504.

(15) Wang, Y.; Xiao, J.; Zhu, H.; Li, Y.; Alsaid, Y.; Fong, K. Y.; Zhou, Y.; Wang, S.; Shi, W.; Wang, Y.; Zettl, A.; Reed, E. J.; Zhang, X. Structural phase transition in monolayer $MoTe_2$ driven by electrostatic doping. *Nature* **2017**, *550*, 487.

(16) Rhodes, D.; Chenet, D. A.; Janicek, B. E.; Nyby, C.; Lin, Y.; Jin, W.; Edelberg, D.; Mannebach, E.; Finney, N.; Antony, A.; Schiros, T.; Klarr, T.; Mazzoni, A.; Chin, M.; Chiu, Y. C.; Zheng, W.; Zhang, Q. R.; Ernst, F.; Dadap, J. I.; Tong, X.; Ma, J.; Lou, R.; Wang, S.; Qian, T.; Ding, H.; Osgood, R. M.; Paley, D. W.; Lindenberg, A. M.; Huang, P. Y.; Pasupathy, A. N.; Dubey, M.; Hone, J.; Balicas, L. Engineering the structural and electronic phases of $MoTe_2$ through W substitution. *Nano Lett.* **2017**, *17*, 1616.

(17) Lv, Y.-Y.; Cao, L.; Li, X.; Zhang, B.-B.; Wang, K.; Bin Pang; Ma, L.; Lin, D.; Yao, S.-H.; Zhou, J.; Chen, Y. B.; Dong, S.-T.; Liu, W.; Lu, M.-H.; Chen, Y.; Chen, Y.-F. Composition and temperature dependent phase transition in miscible $Mo_{1-x}W_xTe_2$ single crystals. *Sci. Rep.* **2017**, *7*, 44587.

(18) Deng, Y.; Li, P.; Zhu, C.; Zhou, J.; Wang, X.; Cui, J.; Yang, X.; Tao, L.; Zeng, Q.; Duan, R.; Fu, Q.; Zhu, C.; Xu, J.; Qu, F.; Yang, C.; Jing, X.; Lu, L.; Liu, G.; Liu, Z. Controlled synthesis of $Mo_{1-x}W_xTe_2$ atomic layers with emergent quantum states. *ACS Nano* **2021**, *15*, 11526−11534.

(19) Zhang, F.; Zhang, H.; Krylyuk, S.; Milligan, C. A.; Zhu, Y.; Zemlyanov, D. Y.; Bendersky, L. A.; Burton, B. P.; Davydov, A. V.; Appenzeller, J. Electric-field induced structural transition in vertical $MoTe_2$- and $Mo_{1-x}W_xTe_2$-based resistive memories. *Nat. Mater.* **2019**, *18*, 55−61.

(20) Allain, A.; Kang, J.; Banerjee, K.; Kis, A. Electrical contacts to two-dimensional semiconductors. *Nat. Mater.* **2015**, *14*, 1195−1205.

(21) English, C. D.; Shine, G.; Dorgan, V. E.; Saraswat, K. C.; Pop, E. Improved contacts to MoS_2 transistors by ultra-high vacuum metal deposition. *Nano Lett.* **2016**, *16*, 3824−3830.

(22) Sung, J. H.; Heo, H.; Si, S.; Kim, Y. H.; Noh, H. R.; Song, K.; Kim, J.; Lee, C. S.; Seo, S. Y.; Kim, D. H.; Kim, H. K.; Yeom, H. W.; Kim, T. H.; Choi, S. Y.; Kim, J. S.; Jo, M. H. Coplanar semiconductor-metal circuitry defined on few-layer $MoTe_2$ via polymorphic heteroepitaxy. *Nat. Nanotechnol.* **2017**, *12*, 1064−1070.

(23) Lee, H. H.; Lim, E.; Kang, S.; Eshete, Y. A.; Won, D.; Lee, Y.; Jeong, J. Y.; Yang, H.; Chiang, C. Y.; Cho, S. Local phase transition at

crack edges of $Mo_{1-x}W_xTe_2$ polymorphs. *Appl. Surf. Sci.* **2022**, *596*, 153503.

(24) Sengupta, R.; Dangi, S.; Krylyuk, S.; Davydov, A. V.; Pavlidis, S. Phase transition of Al_2O_3-encapsulated $MoTe_2$ via rapid thermal annealing. *Appl. Phys. Lett.* **2022**, *121*, 033101.

(25) Zhang, S. C.; Wu, Y.; Gao, F.; Shang, H. M.; Zhang, J.; Li, Z. H.; Fu, Y. Q.; Hu, P. A. Field effect transistor sensors based on in-plane 1T′/2H/1T′ $MoTe_2$ heterophases with superior sensitivity and output signals. *Adv. Funct. Mater.* **2022**, *32*, 2205299.

(26) Xu, X. L.; Liu, S.; Han, B.; Han, Y.; Yuan, K.; Xu, W. J.; Yao, X. H.; Li, P.; Yang, S. Q.; Gong, W. T.; Muller, D. A.; Gao, P.; Ye, Y.; Dai, L. Scaling-up atomically thin coplanar eemiconductor-metal circuitry via phase engineered chemical assembly. *Nano Lett.* **2019**, *19*, 6845−6852.

(27) Yang, S. Q.; Xu, X. L.; Xu, W. J.; Han, B.; Ding, Z. P.; Gu, P. F.; Gao, P.; Ye, Y. Large-scale vertical 1T'/2H $MoTe_2$ nanosheet-based heterostructures for low contact resistance transistors. *ACS Appl. Nano Mater.* **2020**, *3*, 10411−10417.

(28) Xu, X. L.; Pan, Y.; Liu, S.; Han, B.; Gu, P. F.; Li, S. H.; Xu, W. J.; Peng, Y. X.; Han, Z.; Chen, J.; Gao, P.; Ye, Y. Seeded 2D epitaxy of large-area single-crystal films of the van der Waals semiconductor 2H $MoTe_2$. *Science* **2021**, *372*, 195−200.

(29) Li, J.; Yang, X. D.; Liu, Y.; Huang, B. L.; Wu, R. X.; Zhang, Z. W.; Zhao, B.; Ma, H. F.; Dang, W. Q.; Wei, Z.; Wang, K.; Lin, Z. Y.; Yan, X. X.; Sun, M. Z.; Li, B.; Pan, X. Q.; Luo, J.; Zhang, G. Y.; Liu, Y.; Huang, Y.; Duan, X. D.; Duan, X. F. General synthesis of two-dimensional van der Waals heterostructure arrays. *Nature* **2020**, *579*, 368−374.

(30) Zhang, Z. W.; Huang, Z. W.; Li, J.; Wang, D.; Lin, Y.; Yang, X. D.; Liu, H.; Liu, S.; Wang, Y. L.; Li, B.; Duan, X. F.; Duan, X. D. Endoepitaxial growth of monolayer mosaic heterostructures. *Nat. Nanotechnol.* **2022**, *17*, 493−499.

(31) Zhang, Q.; Wang, X. F.; Shen, S. H.; Lu, Q.; Liu, X. Z.; Li, H. Y.; Zheng, J. Y.; Yu, C. P.; Zhong, X. Y.; Gu, L.; Ren, T. L.; Jiao, L. Y. Simultaneous synthesis and integration of two-dimensional electronic components. *Nat. Electron.* **2019**, *2*, 164−170.

(32) Zhang, C. X.; Kc, S.; Nie, Y. F.; Liang, C. P.; Vandenberghe, W. G.; Longo, R. C.; Zheng, Y. P.; Kong, F. T.; Hong, S.; Wallace, R. M.; Cho, K. Charge mediated reversible metal-insulator transition in monolayer $MoTe_2$ and $Mo_{1-x}W_xTe_2$ alloy. *ACS Nano* **2016**, *10*, 7370−7375.

(33) Duerloo, K. A.; Li, Y.; Reed, E. J. Structural phase transitions in two-dimensional Mo- and W-dichalcogenide monolayers. *Nat. Commun.* **2014**, *5*, 4214.

(34) Xu, X. L.; Chen, S. L.; Liu, S.; Cheng, X.; Xu, W. J.; Li, P.; Wan, Y.; Yang, S. Q.; Gong, W. T.; Yuan, K.; Gao, P.; Ye, Y.; Dai, L. Millimeter-scale single-crystalline semiconducting $MoTe_2$ via solidto-solid phase transformation. *J. Am. Chem. Soc.* **2019**, *141*, 2128−2134.

(35) Song, S.; Sim, Y.; Kim, S.-Y.; Kim, J. H.; Oh, I.; Na, W.; Lee, D. H.; Wang, J.; Yan, S.; Liu, Y.; Kwak, J.; Chen, J.-H.; Cheong, H.; Yoo, J.-W.; Lee, Z.; Kwon, S.-Y. Wafer-scale production of patterned transition metal ditelluride layers for two-dimensional metal−semiconductor contacts at the Schottky−Mott limit. *Nat. Electron.* **2020**, *3*, 207−215.